

Facile patterning of electrospun polymer fibers enabled by electrostatic lensing interactions

Kirill Titov and Jin-Chong Tan^a

Multifunctional Materials & Composites (MMC) Laboratory, Department of Engineering Science, University of Oxford, Parks Road, OX1 3PJ Oxford, United Kingdom

(Received 24 June 2016; accepted 2 August 2016; published online 16 August 2016)

Hierarchical polymer fibers with long-range ordering have been straightforwardly fabricated employing a macroscale patterned mesh comprising microscale metallic filaments as a conductive collector, in an otherwise conventional electrospinning apparatus. Using electrostatic simulations, we elucidate that the patterning electric field is extremely confined to the immediate vicinity of the mesh collector surface. This lensing phenomenon is controlling the fiber patterning effect, and its strength decays with height above the patterned surface. Our study sheds new light on the physical mechanism underpinning electrospinning and offers a new approach for engineering fiber architectures where a precise control of in-plane physical properties is sought. © 2016 Author(s). All article content, except where otherwise noted, is licensed under a Creative Commons Attribution (CC BY) license (<http://creativecommons.org/licenses/by/4.0/>). [<http://dx.doi.org/10.1063/1.4960982>]

Electrospinning is a remarkably versatile method to yield fine-scale fibers,^{1,2} architected membranes,^{3,4} and novel nanocomposites,^{5–7} utilizing a vast range of contemporary polymeric materials.⁸ There is an enormous current interest to develop innovative technologies based on electrospun fibers, aimed at a myriad of practical applications, encompassing optoelectronics and sensors,^{9–11} filtrations and capture,¹² tissue engineering,¹³ drug delivery, and biomedicine.¹⁴ However, at the heart of the electrospinning process lies an *instability*, which gives the fibers their unique properties. This letter advances our current understanding of the physical mechanisms for harnessing this material instability, which thus far remained a fundamental challenge for unlocking the full potential of electrospinning.

The electrospinning process extracts a jet of polymer solution from an emitter (usually a blunt tip needle) and accelerates it using a strong electric field. As the jet leaves the emitter, it travels in a straight line for a short distance until the onset of the whipping instability (snapshot shown in the inset of Fig. 1(a); high speed video in the [supplementary material](#)), which is responsible for thinning the jet down by two orders of magnitude.¹⁵ This instability makes collecting the forming fibers in an ordered manner highly challenging without dramatically reducing productivity as in electrohydrodynamic direct-writing, or “near-field” electrospinning, which does away with the instability and deposits a straight jet in a manner mimicking filament 3D printing.¹⁶ In the light of this, there is a considerable current interest in the development of innovative collector designs capable of guiding precise deposition of electrospun fibers.¹⁷ The study presented in this letter addresses this challenge in a way that does not suffer from disadvantages of “near-field” electrospinning.

One of the simplest methods involves electrospinning onto two grounded parallel strips of conductor separated by a gap, thereby aligning fibers perpendicular to the conductors.¹⁸ This effect is achieved by modifying the shape of the electric field established between the emitter and the collector, affecting the pathway taken by the forming fibers relatively close to the collector surface. This basic approach has been studied as a go-to for making aligned fibers^{19–22} and found application in nanofiber device production.²³ However, collecting the desired fibers in the gaps (distance of the order of ~mm) is inefficient since most fibers are deposited (and wasted) on the highly attractive

^aE-mail: jin-chong.tan@eng.ox.ac.uk



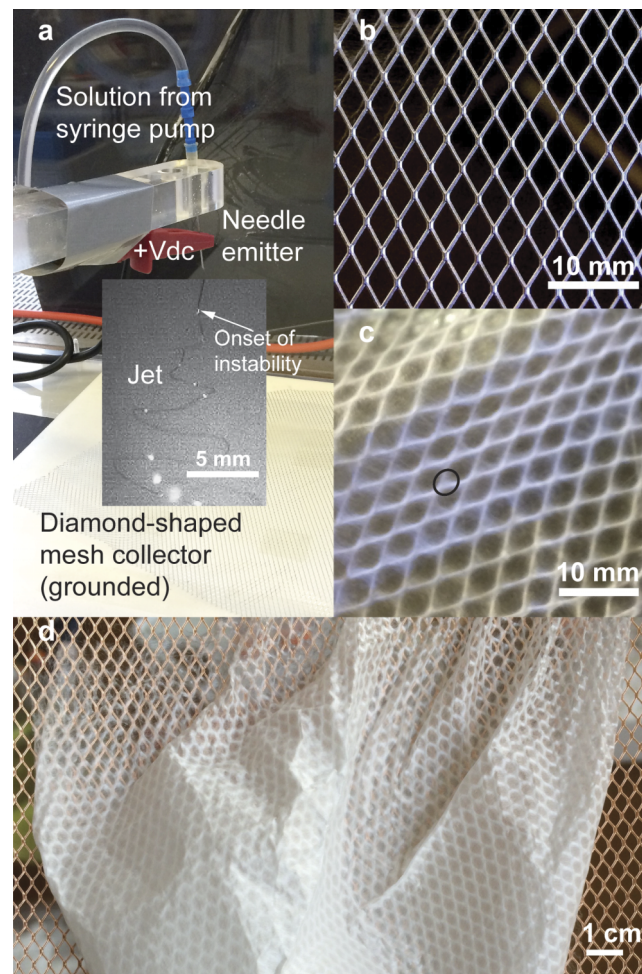


FIG. 1. Photographs of (a) the electrospinning apparatus used in this study with inset snapshot of the polymer solution jet, (b) diamond-patterned aluminum mesh functioning as the ground collector, (c) close-up macroscopic image of a sample of PVP fiber mat mimicking the patterned collector geometry, where the black oval highlights an increase in fiber density inside the acute angles of the diamond-shaped cells, and (d) large-scale view of a sample of PVP fiber mat shown here detached from a diamond-patterned copper mesh. (Multimedia view) [URL: <http://dx.doi.org/10.1063/1.4960982.1>]

conductor surfaces.¹⁷ The technique of changing the topography of the collector has been extended to variously shaped meshes and assemblies, as exemplified by a number of recent publications.^{24–27} Further structuring of the architecture of the fiber mat has also been attempted on a much finer length scale. For instance, by using photolithographically micro-patterned collectors with patterned features: as small as 40- μm protrusions from a flat conductive surface.¹³

The work presented in this letter bridges the gap between the aforementioned two ends of the spectrum (viz., straddling μm to mm length scales), elucidating the simple concept of a collector with macroscopic shapes constructed from a 400 μm wide wire filaments (Figs. 1(b) and 1(d)). We demonstrate that the relatively fine scale geometry of a diamond-shaped mesh collector is imparting a significant “electric field lensing” effect upon fiber deposition, thereby enabling facile fabrication of highly ordered fibrous mats. Importantly our work advances the basic understanding of how to control the aggressively whipping electrospinning jet, without sacrificing the overall material productivity or limiting potential improvements in productivity using novel emitter designs.^{28,29}

The electrospinning polymer solution was prepared by dissolving polyvinylpyrrolidone (PVP) powder with an average molecular weight of $M_w \sim 1\,300\,000$ in methanol (MeOH), both acquired from Sigma-Aldrich Co. Solutions containing 15–20 wt. % of PVP in MeOH were successfully used to electrospin good quality continuous fibers, with diameters ranging from 2 to 4 μm depending

on the processing parameters used. The solution was supplied to the G19 needle emitter (nozzle) with a blunt tip via a syringe pump at a flow rate of 0.5 to 2 ml h⁻¹. The needle was positioned at ~15 cm (Fig. 1(a)) above the diamond-shaped (Al or Cu) mesh collector (Fig. 1(b)). Positive polarity voltages of 6–10 kV were applied to the needle depending on solution concentration and flow rate. Each fiber mat was deposited in ~10 min (see time-lapse video of fiber mat build-up in the [supplementary material](#)), generating a nominal thickness of ca. 200–300 μm without the loss of patterned architecture. The thickness of the achievable well-ordered layer was estimated using the Alicona Infinite Focus profilometer and a representative profile is given in Fig. S7 of the [supplementary material](#). The microstructure and orientation of the fibers were characterized using a scanning electron microscope (Carl Zeiss EVO LS15 SEM). A custom-built MATLAB routine based on the Hough transform algorithm³⁰ was implemented to analyze the SEM images for determination of fiber alignment.

The result of electrospinning onto this diamond-shaped (hereafter termed “diamond”) mesh is a non-woven sheet of micro-scale fibers that mimic the architecture of the mesh collector, whose macroscopic images are shown in Fig. 1. SEM images are shown in Fig. 2(a) (additional images in the [supplementary material](#)), revealing that the walls of the diamond unit cells in the PVP fiber mat architecture are comprising fibers preferentially aligned along the wires; see inset of Fig. 2(a) and the [supplementary material](#). Fiber orientation was measured on 14 walls of the same sample, with images taken in regions similar to that indicated by the white rectangle marked in Fig. 2(a). The histogram in Fig. 2(b) summarizes the results, to which a normal distribution of fiber orientation (θ) relative to the wall local axis has been fitted giving resulting parameters: $\mu = 3.4^\circ$, $\sigma = 17.8^\circ$. In contrast, the fibers occupying the gaps are randomly oriented. However, it is evident that fiber concentration is higher in regions adjacent to the acute angles of the diamond-shaped unit cells, as indicated by the white oval in Fig. 2(a). This effect is also apparent in the macroscopic images, marked by the black oval in Fig. 1(c). We shall elucidate that the observed nature of differential alignments and this increase of local density are a response of fiber deposition dynamics to the underpinning electrostatics.

To understand the underlying mechanism responsible for this micro- to macro-scale patterning phenomena, we constructed 3-D Computer Aided Design (CAD) models (Figs. 3(a) and 3(b)) of the “needle emitter to mesh collector” (needle-mesh) system and that of a *basic* “needle emitter to plate collector” (needle-plate) system, and the latter is widely used in standard electrospinning setups; we then applied finite-element (FE) modeling (COMSOL Multiphysics) to simulate and compare the governing electrostatic fields of both systems (Figs. 3(c)–3(h)). Three major insights spring from this comparison: (i) the horizontal components of the electric field are responsible for the observed fiber patterning effect; (ii) there is practically no difference between the needle-mesh and the needle-plate configurations in terms of the electric field “seen” by the electrospinning jet when approaching “far away” from the collector; (iii) the patterning field strength decays exponentially with height (z -axis).

Fig. 2(a) shows the vector field of the horizontal components of the governing electric field sampled at specific heights of 0.05 mm, 0.5 mm, and 1 mm above the collector top surface, and superimposed onto a micrograph of the resulting fibers. The magnitude of the component perpendicular to the long-axis of the mesh joints (E_x) was sampled across 12 diamond-shaped unit cells along the centerline depicted in Fig. 2(a), along which the other horizontal component is negligible, and compared to the magnitude of the vertical component (E_z) at the corresponding points. The results are summarized in Fig. 2(c). Notably we established that at heights below 1 mm, E_x is of the same order of magnitude as E_z , which indicates that the horizontal component has a significant effect on the dynamics of the electrospinning jet *nearby* patterned collector surface. Moreover, Fig. 2(a) shows an excellent agreement between the shape of the electric field near the collector surface and the architecture of the underlying fiber mesh obtained. It is striking to see that, the regions in the diamond cell gaps where E_{x-y} is comparatively weaker as evidenced here by the relatively smaller field vectors (marked by white oval) indeed show a relatively higher concentration of fibers, as highlighted above.

A larger scale view is presented in Fig. 3 comparing the electric field experienced by the electrospinning jet along the whole pathway (between emitter and collector) in the needle-plate

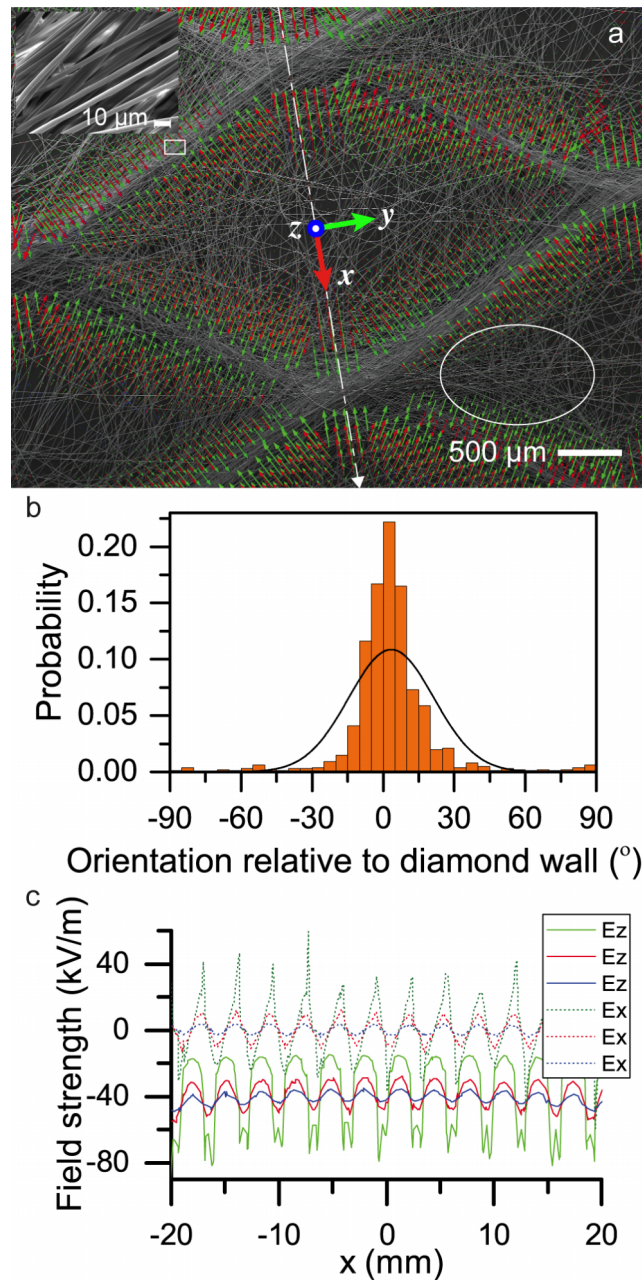


FIG. 2. (a) Micrograph of a diamond-shaped unit cell of a patterned PVP fiber mat with a superimposed vector fields corresponding to the horizontal component of the driving electric field sampled at 0.05 mm (green), 0.5 mm (red), and 1 mm (blue) above the surface of the collector mesh. Note that the blue arrows are almost indiscernible due to scaling with electric field strength, magnitudes elucidated in (c). The inset shows the representative aligned fibers on the walls of the diamond cell taken at the area indicated by the white rectangle. (b) Histogram of the fiber alignment on the diamond cell walls confirming its strong preferred orientation, and the line is the fitted normal distribution. (c) Vertical (z-component) and horizontal (x-component) electric field strengths determined from finite-element calculations at 8 kV applied voltage, sampled along the white center line (x-axis) across several diamond unit cells; color code as in (a). (Multimedia view) [URL: <http://dx.doi.org/10.1063/1.4960982.2>]

versus the needle-mesh systems. The two systems were simulated with the same bulk dimensions employing an identical 8 kV positive voltage applied to the needle emitter. Because of symmetry, it is sufficient to consider the horizontal E_y slices in Figs. 3(a)-3(f) to gain insight into the underscoring field shapes (see corresponding E_z and E_x contours in the [supplementary material](#), as well as

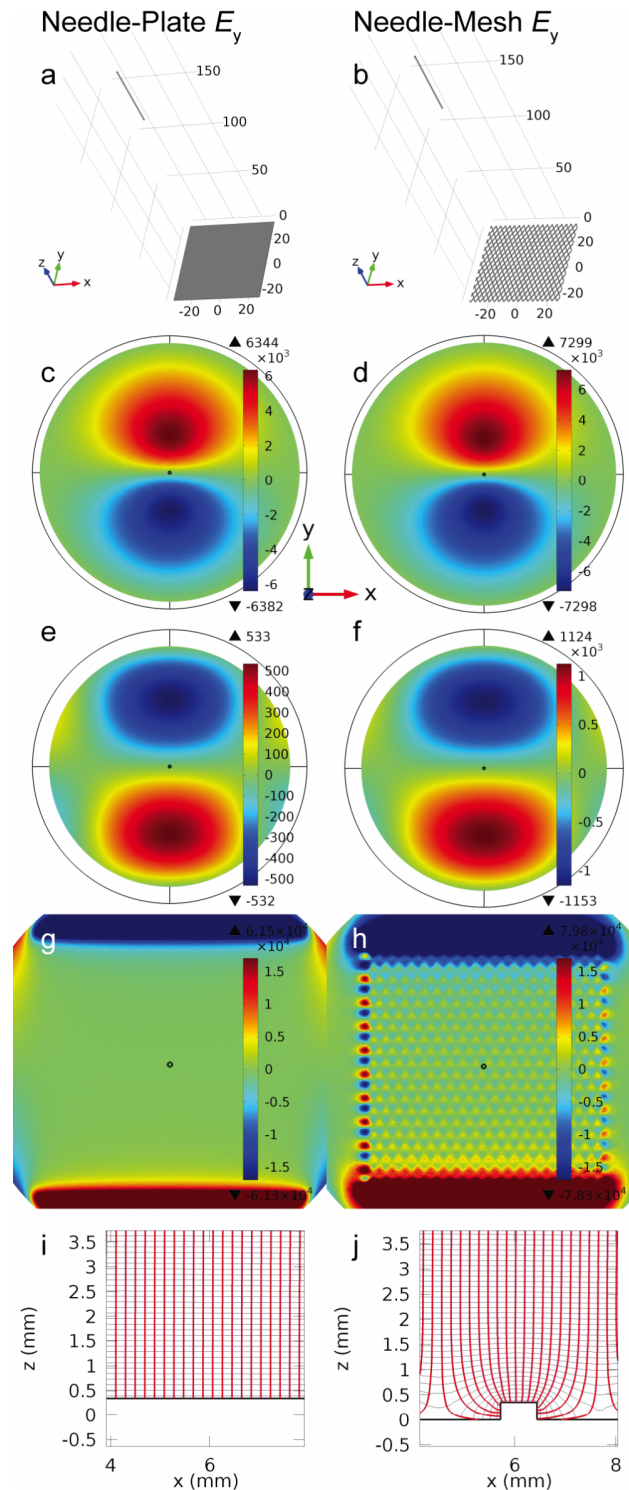


FIG. 3. Comparison of finite-element (FE) electric field simulation results. A needle-plate system (a) is compared to a needle-mesh system (b), both of which have matching geometries and simulated at 8 kV applied voltage. Horizontal plane slices of one horizontal component (along the y -axis) of the governing electric field (E_y in V m^{-1}) are shown at heights of ((c) and (d)) 135 mm, ((e) and (f)) 40 mm, and ((g) and (h)) 1 mm above the top surface of the base collector. Equipotential contours (thin blue) and E_{x-z} electric field lines (red) of a vertical section in a $z-x$ plane of the “lensing” regions are plotted for the (i) needle-plate and (j) needle-mesh systems (slice through the joints of the diamond-shaped mesh). It is noted that the electric field switches direction between panels ((c) and (d)) and ((e) and (f)) because, at a height of ~ 60 mm, the horizontal field is effectively zero, at which point the field stops diverging the jet and starts pulling it back in towards the collector.

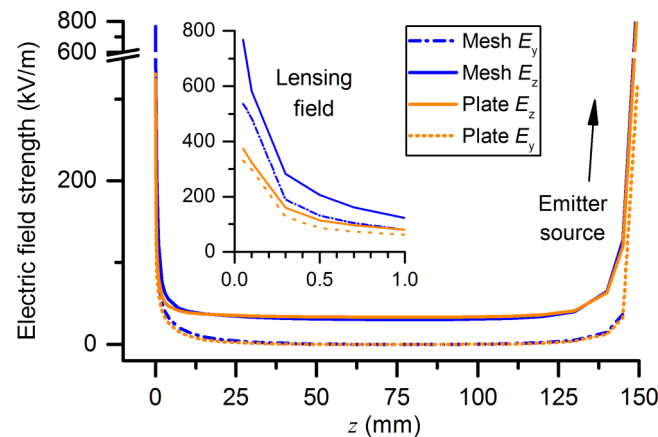


FIG. 4. The maximum field strength predicted from FE simulations, showing the vertical (z) and horizontal (y) components sampled at a range of heights for comparison between the needle-mesh versus the needle-plate systems. The inset depicts the strong lensing effects under the height of 1 mm.

additional E_x and E_y at heights of 0.5 mm and 0.05 mm above collector surface). Notably we discovered that the electric fields become dissimilar only *near* the collector surface. Furthermore, the maximum vertical (E_z) and horizontal (E_y) field strengths are shown as a function of heights above the collector surface in Fig. 4; it can be seen that the fields in the needle-plate and the needle-mesh systems are similar in magnitude as well as shape. On this basis, because the electrospinning jet experiences similar electric fields until it is getting very close to the collector surface in both configurations, it is evident that the highly localized electrostatic lensing interaction established at the proximity of the mesh collector, in fact, is controlling the precise patterning of the fiber mats in the needle-mesh system.

Patterned metal mesh is thus shown to effectively act as an “electrostatic lens” focusing fiber deposition onto the conductive walls of the periodic diamond cells, by means of electrostatic attraction between the solidified charged electrospinning jet and the grounded surface. Most fibers are strongly attracted to the diamond walls along a significant portion of fiber length and converge in a highly ordered manner onto the walls; while only those fibers, whose path dynamics are significantly unfavorable for deposition onto the collector walls, are randomly stranded amongst the gaps. We note that, when the mat thickness increases (exceeding $\sim 500\ \mu\text{m}$), however, there is progressively less space for ordering the depositing fibers in the region of the strong horizontal field E_{x-y} . Consequently, we found that fewer fibers are dynamically well positioned for aligned deposition, leading to more fibers depositing in an increasingly disordered fashion. Another cause of this increasing disorder is the residual charge left in the deposited fibers,³¹ which may distort the lensing electric field. This effect, however, is strongly material and process parameter dependent. The patterning of the fiber mat thus becomes “blurred” when the deposited mat thickness starts to build up. Fig. 1(c) depicts a thinner mat with a clearly defined architecture, while the sample in Fig. 1(d) has regions towards the center of the mat where the gaps are significantly more opaque than towards the edge of the mat, which is the result of fiber deposition becoming more randomly isotropic (see micrographs in Fig. S6 of the [supplementary material](#)). This observation is consistent with our FE simulations presented above. Particularly, we revealed that (i) the horizontal field strength in Fig. 2(c) has declined by an order of magnitude at heights as close to the collector surface as $\sim 1\ \text{mm}$, and (ii) the steep negative gradient in Fig. 4 indicating a large reduction of the maximum E_y field strength with increasing height from the collector surface. Whilst this might appear to be the main limitation of the patterned collector approach, it is not detrimental for functional applications where a large thickness of the fiber mat is not a major requirement. It may also be possible to increase the achievable thickness of the well-ordered fiber mat via electrospinning using both a positive and a negative applied voltage intermittently, as proposed in this study.³² Further work in this direction will be warranted.

The fundamental physical mechanism revealed in this letter provides an efficient method to achieve highly ordered polymer fiber mats via electrostatic lensing electrospinning, by leveraging the concept of conductive patterned collectors. It is envisaged that the elucidated lensing effect can allow for fine-tuning, via specific patterning of the fiber mat with various shapes and sizes (e.g., rectangular, circular, and honeycomb), of a range of in-plane physical properties, such as to control the mechanical behavior and electro-thermal transport characters of electrospun mats resembling those in metal honeycombs.³³ There is a huge scope for exciting new applications, for instance, precise guidance of nerve cell growth along the aligned fibers to afford nerve tissue engineering.³⁴ Intriguingly by constructing a macro-level architecture using a micro-scale geometry, we show that it is possible to precisely deposit fine-scale electrospun fibers without sacrificing the processing productivity, which bodes well for complementing current trends in development of high-throughput emitter designs.^{28,29,35,36} Electrostatic lensing is a simple yet extremely powerful approach, to enrich the repertoire available to the rapidly expanding field of electrospinning of multiscaled materials.

See [supplementary material](#) for additional SEM micrographs and FE model predictions.

J.-C.T. would like to acknowledge the Engineering and Physical Sciences Research Council (EPSRC) RCUK (Grant Nos. EP/K031503/1 and EP/N014960/1) for the provision of research funding. We are grateful to the Oxford John Fell Fund (No. 151/120) and the Balliol's Lubbock Grant (No. 2014b/3) for small equipment support. Additional data can be accessed via ORA (<http://ora.ouls.ox.ac.uk>). Request for any material samples or specimens described in this manuscript should be directed to the corresponding author.

- ¹ S. V. Fridrikh, J. H. Yu, M. P. Brenner, and G. C. Rutledge, *Phys. Rev. Lett.* **90**(14), 144502 (2003).
- ² I. Coluzza, D. Pisignano, D. Gentili, G. Pontrelli, and S. Succi, *Phys. Rev. Appl.* **2**(5), 054011 (2014).
- ³ D. Zhang and J. Chang, *Nano Lett.* **8**(10), 3283 (2008).
- ⁴ J. Y. Chen, H. C. Wu, Y. C. Chiu, and W. C. Chen, *Adv. Energy Mater.* **4**(8), 1301665 (2014).
- ⁵ R. Ostermann, J. Cravillon, C. Weidmann, M. Wiebcke, and B. M. Smarsly, *Chem. Commun.* **47**(1), 442 (2011).
- ⁶ Z.-M. Huang, Y. Z. Zhang, M. Kotaki, and S. Ramakrishna, *Compos. Sci. Technol.* **63**(15), 2223 (2003).
- ⁷ X. Li, X. Yu, C. Cheng, L. Deng, M. Wang, and X. Wang, *ACS Appl. Mater. Interfaces* **7**(39), 21919 (2015).
- ⁸ G. R. Mitchell, *Electrospinning: Principles, Practice and Possibilities* (Royal Society of Chemistry, 2015).
- ⁹ A. J. Das, C. Lafargue, M. Lebental, J. Zyss, and K. S. Narayan, *Appl. Phys. Lett.* **99**(26), 263303 (2011).
- ¹⁰ X. Y. Wang, C. Drew, S. H. Lee, K. J. Senecal, J. Kumar, and L. A. Samuelson, *Nano Lett.* **2**(11), 1273 (2002).
- ¹¹ X. Mao, F. Simeon, G. C. Rutledge, and T. A. Hatton, *Adv. Mater.* **25**(9), 1309 (2013).
- ¹² F. Bai, J. Wu, G. Gong, and L. Guo, *Adv. Sci.* **2**(7), 1500047 (2015).
- ¹³ S. Nedjari, S. Eap, A. Hebraud, C. R. Wittmer, N. Benkirane-Jessel, and G. Schlatter, *Macromol. Biosci.* **14**(11), 1580 (2014).
- ¹⁴ S. M. Damaraju, S. Wu, M. Jaffe, and T. L. Arinzeh, *Biomed. Mater.* **8**(4), 045007 (2013).
- ¹⁵ C. J. Thompson, G. G. Chase, A. L. Yarin, and D. H. Reneker, *Polymer* **48**(23), 6913 (2007).
- ¹⁶ Y. Huang, N. Bu, Y. Duan, Y. Pan, H. Liu, Z. Yin, and Y. Xiong, *Nanoscale* **5**(24), 12007 (2013).
- ¹⁷ W. E. Teo and S. Ramakrishna, *Nanotechnology* **17**(14), R89 (2006).
- ¹⁸ D. Li, Y. L. Wang, and Y. N. Xia, *Nano Lett.* **3**(8), 1167 (2003).
- ¹⁹ H. Yan, L. Q. Liu, and Z. Zhang, *Appl. Phys. Lett.* **95**(14), 143114 (2009).
- ²⁰ J. Rafique, J. Yu, J. Yu, G. Fang, K. W. Wong, Z. Zheng, H. C. Ong, and W. M. Lau, *Appl. Phys. Lett.* **91**(6), 063126 (2007).
- ²¹ G. Kim and W. Kim, *Appl. Phys. Lett.* **88**(23), 233101 (2006).
- ²² J. R. Y. Stevenson, S. Lattante, P. André, M. Anni, and G. A. Turnbull, *Appl. Phys. Lett.* **106**(17), 173301 (2015).
- ²³ Y. K. Fuh and L. C. Lien, *Nanotechnology* **24**(5), 055301 (2013).
- ²⁴ C. Vaquette and J. J. Cooper-White, *Acta Biomater.* **7**(6), 2544 (2011).
- ²⁵ Y. Wu, Z. Dong, S. Wilson, and R. L. Clark, *Polymer* **51**(14), 3244 (2010).
- ²⁶ S. Zhao, Q. Zhou, Y. Z. Long, G. H. Sun, and Y. Zhang, *Nanoscale* **5**(11), 4993 (2013).
- ²⁷ D. Zhang and J. Chang, *Adv. Mater.* **19**(21), 3664 (2007).
- ²⁸ I. Bhattacharyya, M. C. Molaro, R. D. Braatz, and G. C. Rutledge, *Chem. Eng. J.* **289**, 203 (2016).
- ²⁹ X. Yan, J. Marini, R. Mulligan, A. Deleault, U. Sharma, M. P. Brenner, G. C. Rutledge, T. Freyman, and Q. P. Pham, *PLoS One* **10**(5), e0125407 (2015).
- ³⁰ See <http://uk.mathworks.com/help/images/ref/hough.html> for Modified Hough Transform.
- ³¹ G. Collins, J. Federici, Y. Imura, and L. H. Catalani, *J. Appl. Phys.* **111**(4), 044701 (2012).
- ³² H.-W. Tong and M. Wang, *Mater. Lett.* **94**, 116 (2013).
- ³³ A. J. Wang and D. L. McDowell, *J. Eng. Mater. Technol.* **126**(2), 137 (2004).
- ³⁴ W. Zhu, F. Masood, J. O'Brien, and L. G. Zhang, *Nanomed. Nanotechnol. Biol. Med.* **11**(3), 693 (2015).
- ³⁵ G. Jiang and X. Qin, *Mater. Lett.* **128**, 259 (2014).
- ³⁶ Z. Liu, R. X. Chen, and J. H. He, *Mater. Des.* **94**, 496 (2016).